aerospace

MDPI

Article

Effects of Characteristic Chamber Length on c^* Efficiency in CAMUI-Type Hybrid Rockets Using Hydrogen Peroxide

Ryota Kinjo [1], Sota Watanabe [1], Ananda Rafi Dhaifan [1], Masashi Wakita [2] and Harunori Nagata [2,*]

[1] Graduate School of Engineering, Division of Mechanical and Space Engineering, Hokkaido University, Sapporo 060-8628, Japan; kinjo.ryota.k1@elms.hokudai.ac.jp (R.K.); watanabe.souta.l3@elms.hokudai.ac.jp (S.W.); rafidhaifan.ananda.w0@elms.hokudai.ac.jp (A.R.D.)
[2] Faculty of Engineering, Division of Mechanical and Space Engineering, Hokkaido University, Sapporo 060-8628, Japan; m-wakita@eng.hokudai.ac.jp
* Correspondence: nagata@eng.hokudai.ac.jp

Abstract

This study experimentally investigated the effect of characteristic chamber length, L^*, on combustion efficiency and stability in CAMUI-type hybrid rockets using 70 wt% and 80 wt% hydrogen peroxide under non-catalytic spray-injection conditions. Combustion tests were conducted by systematically varying L^* through changes in the nozzle throat diameter while maintaining the combustor volume constant. For both oxidizer concentrations, the characteristic exhaust velocity efficiency, η_{c^*}, increased with increasing L^*. The 70 wt% cases required a larger L^* than the 80 wt% cases to achieve comparable efficiency, and flame blowoff occurred in the low-L^* region. The normalized RMS pressure fluctuation was also larger for the 70 wt% cases, particularly in the low-L^* region, indicating lower combustion stability. These results indicate that reducing the hydrogen peroxide concentration increases the L^* required to maintain stable and efficient combustion. As a key outcome of this study, stable and efficient combustion of 70 wt% hydrogen peroxide was demonstrated without catalytic assistance when a sufficiently large L^* was provided. These results demonstrate the capability of the CAMUI-type combustor to extend stable operation toward lower oxidizer concentrations and experimentally clarify the concentration-dependent L^* requirement as a practical design guideline for catalyst-free hydrogen peroxide hybrid rockets.

Keywords: hybrid rocket; hydrogen peroxide; CAMUI-fuel; c^* efficiency; combustion stability

Check for updates

Academic Editor: Jae Hyun Park

Received: 30 April 2026
Revised: 1 June 2026
Accepted: 2 June 2026
Published: 4 June 2026

Copyright: © 2026 by the authors. Licensee MDPI, Basel, Switzerland. This article is an open access article distributed under the terms and conditions of the Creative Commons Attribution (CC BY) license.

1. Introduction

The demand for launching small spacecraft has rapidly increased with the expansion of applications such as Earth observation, communications, technology demonstration, and support for deep-space exploration [1]. Consistent with this trend, BryceTech reported that 4544 spacecraft were deployed in 2025, with smaller satellites weighing less than 1200 kg accounting for 98% of spacecraft launched that year [2]. However, simply increasing the number of dedicated launch opportunities is not straightforward because launch-vehicle manufacturing, launch-site operations, safety reviews, and launch coordination require substantial cost and time. Therefore, rideshare launch opportunities using the excess payload capacity of large launch vehicles have become an important means of providing access to space for multiple small spacecraft. At the same time, rideshare launches generally impose constraints on the orbital conditions available to secondary payloads. Since the target orbit and launch schedule are primarily determined by the mission requirements

of the primary payload, small spacecraft carried as secondary payloads are not always injected directly into their desired orbits [3]. As a result, their freedom in selecting orbital altitude, inclination, phase, and launch timing is limited. For future small spacecraft to conduct more advanced and independent missions, it will become increasingly important for them to carry onboard propulsion systems capable of orbit transfer, orbit adjustment, and deorbiting after separation from the launch vehicle.

Existing propulsion systems have clear advantages, but they also present limitations when applied to rideshare spacecraft. Electric propulsion offers very high specific impulse and can achieve large total velocity increments with a limited propellant mass [4]. However, its low thrust level results in long maneuvering times for significant orbital changes, making it unsuitable for missions that require rapid orbit transfer or early arrival at a target orbit after deployment. In contrast, chemical propulsion systems, such as liquid and solid rockets [4], can generate high thrust and are advantageous for short-duration orbital maneuvers. However, many conventional liquid chemical propulsion systems use toxic or highly reactive propellants, such as hydrazine-based fuels and nitrogen tetroxide-based oxidizers, which impose severe safety constraints on ground handling, launch-site operations, and compatibility with other payloads in rideshare missions. Solid rocket motors are structurally simple and can provide high thrust, but the fuel and oxidizer are premixed in an energetic solid propellant, raising safety concerns associated with accidental ignition or explosion [4]. In addition, the difficulty of shutdown and thrust control after ignition limits their applicability to small spacecraft propulsion. For small spacecraft, the relative impact of safety-related cost is particularly important. Even if the propulsion system itself is small, the cost and procedures required for safety review, storage, transportation, ground handling, and launch-site operation do not necessarily decrease in proportion to spacecraft size when hazardous propellants are involved. Consequently, as the spacecraft becomes smaller, the relative burden of safety management can become a larger fraction of the overall mission cost and complexity. Therefore, propulsion systems for small spacecraft must not only provide sufficient performance, but also offer excellent safety, handling characteristics, and storability.

Hybrid rockets are promising candidates for addressing these requirements. Hybrid rockets typically employ propellants in different phases, most commonly a solid fuel and a liquid or gaseous oxidizer. This configuration offers several advantages: (1) the solid fuel is relatively easy to handle because it is chemically stable by itself; (2) the separation of fuel and oxidizer reduces the possibility of unintended energetic reactions before ignition; (3) shutdown, restart, and thrust modulation can be realized by controlling the oxidizer supply; and (4) the propulsion system can be simplified because only the oxidizer side requires a feed system [5]. These characteristics make hybrid rockets attractive candidates for post-boost stages and kick motors for small spacecraft [6].

Hydrogen peroxide (H_2O_2) has attracted attention as a low-toxicity propellant and is also a promising oxidizer for hybrid rockets. Hydrogen peroxide decomposes into water and oxygen, and is therefore more environmentally benign than conventional toxic propellants such as hydrazine-based fuels and nitrogen tetroxide-based oxidizers. In addition, highly concentrated hydrogen peroxide has a wide liquid-phase temperature range; for example, 90 wt% hydrogen peroxide has a melting point of approximately −11 °C and a boiling point of approximately 141 °C. It also has a high density, with a specific gravity of approximately 1.45 at 90 wt%, which is advantageous from the viewpoints of storability and system compactness [7]. These characteristics make hydrogen peroxide a suitable oxidizer candidate for compact hybrid rocket motors, including post-boost stages and kick motors for small spacecraft.

https://doi.org/10.3390/aerospace13060528

Recent studies on hydrogen peroxide hybrid rockets have mainly focused on high-test peroxide, typically in the range of 87.5–98 wt%, and have investigated various approaches to improve combustion performance and operability. These approaches include throttleable operation [8], annular-gap injection [9], multiport fuel grains [10], vortex or swirl injection [11,12], hypergolic solid fuels [13], and optimization of hydrogen peroxide injection schemes [14]. Flight-demonstration-oriented developments have also been reported, such as the ILR-33 AMBER using 98 wt% hydrogen peroxide with a catalyst bed and the Nammo Nucleus using 87.5 wt% hydrogen peroxide with a silver catalyst bed [15,16]. These studies demonstrate the increasing maturity of hydrogen peroxide hybrid propulsion. At the same time, they indicate that current hydrogen peroxide hybrid rocket developments are still largely based on high-concentration hydrogen peroxide, catalytic decomposition, or advanced injector and fuel-grain configurations to achieve stable ignition and combustion. For long-duration applications, two issues are particularly important: catalyst-related constraints in decomposition-based operation and oxidizer concentration degradation during storage.

First, catalytic decomposition, which has commonly been employed in hydrogen peroxide hybrid rockets, introduces additional constraints into the propulsion system. In this method, liquid hydrogen peroxide is decomposed in a catalyst bed to generate a high-temperature mixture of steam and oxygen, which promotes ignition of the solid fuel. Kang reported that, for decomposition-based ignition of hydrogen peroxide hybrid rockets, the catalyst bed must provide sufficient decomposition performance while maintaining a low internal pressure drop; otherwise, the required oxidizer inlet pressure can become excessively high [17]. In addition, catalyst beds for highly concentrated hydrogen peroxide are exposed to severe thermal environments. Parzybut et al. noted that decomposition of higher-concentration hydrogen peroxide exposes catalysts to higher temperatures and thermal shocks, and that conventional silver catalysts may suffer from washout or creep when used with 98 wt% hydrogen peroxide [18]. Recent studies have also shown that catalyst support materials and catalyst particle size affect sample degradation, pressure drop, thermomechanical resistance, and ageing of catalyst beds [19,20]. Therefore, achieving stable combustion between hydrogen peroxide and solid fuel without relying on catalytic decomposition is important for simplifying the propulsion system and reducing catalyst-related reliability concerns.

Second, hydrogen peroxide itself can undergo spontaneous decomposition during long-term storage, and the resulting concentration decrease may become non-negligible depending on storage conditions [7]. Such concentration loss affects combustion stability, making it an important constraint for long-duration operation. Although modern purification and handling technologies have greatly improved the storability of hydrogen peroxide [21], spontaneous decomposition cannot be completely eliminated. Therefore, when long-duration missions are considered, it is important to clarify whether stable and efficient combustion can be maintained even after possible oxidizer concentration degradation.

Maintaining stable ignition and combustion at medium or lower peroxide concentrations remains challenging. Wernimont et al. conducted combustion tests using hydrogen peroxide and polyethylene fuel with catalytic ignition and reported successful ignition and flame holding at peroxide concentrations up to 85 wt%, whereas stable combustion was not achieved at 80 wt% under their test conditions [22]. Whitmore et al. demonstrated hybrid rocket combustion using 80 wt% hydrogen peroxide by combining catalytic decomposition with supplemental gaseous oxygen injection; however, they reported combustion-instability issues and discontinued this operating approach [23]. These results indicate that, near 80 wt% hydrogen peroxide, stable combustion is difficult to maintain without assistance such as catalytic decomposition or supplemental oxidizer addition, and that combustion

stability can remain problematic even when such assistance is employed. Thus, for medium- or lower-concentration hydrogen peroxide, stable combustion using conventional fuel-grain configurations remains difficult to demonstrate, particularly without catalytic or supplemental oxidizer assistance.

The CAMUI (CAscaded MUltiple Impinging-jet) [24] fuel-grain configuration is a promising concept for addressing this issue. A schematic of the CAMUI fuel grain is shown in Figure 1. In the CAMUI-type fuel grain, multiple fuel blocks are stacked axially, and adjacent blocks are arranged with a 90-degree phase shift, thereby generating impinging jets and recirculating flow in the combustor. These flow structures enhance heat transfer to the fuel surface and promote mixing between the oxidizer and fuel-rich gas. The effectiveness of the CAMUI configuration for low-concentration hydrogen peroxide has also been suggested in previous combustion experiments. Wakita et al. applied 60 wt% hydrogen peroxide to a CAMUI-type hybrid rocket and verified flame holding by using oxygen assist [25]. They also reported that, under the tested assisted-combustion conditions, the CAMUI-type fuel contributed significantly to the reaction of 60 wt% hydrogen peroxide compared with a cylindrical fuel grain. These results suggest that the impinging-jet and recirculating-flow structures of the CAMUI configuration are effective for promoting the reaction of lower-concentration hydrogen peroxide. Recent experimental and numerical investigations of CAMUI-type fuel configurations have further shown that sequential jet impingement promotes intense mixing and increases the residence time of the reacting flow, resulting in high combustion efficiency and robust, repeatable combustion behavior [26]. Therefore, the CAMUI configuration is expected to promote combustion completion and improve combustion stability even under non-catalytic spray-injection conditions using medium- or lower-concentration hydrogen peroxide.

The objective of the present study is to experimentally identify, within the present test matrix, the lower-limit L^* conditions under which stable combustion and high characteristic exhaust velocity efficiency can be maintained in catalyst-free hydrogen peroxide hybrid rockets for each oxidizer concentration, with particular emphasis on lower-concentration hydrogen peroxide, for which stable combustion is expected to become more difficult. In a CAMUI-type fuel grain, flame stability near the stagnation regions formed by impinging jets is strongly related to the local residence-time scale. For stagnation-point-type flows, this local residence-time scale can be characterized by the inverse of the velocity-gradient scale near the stagnation region. Since the characteristic chamber length, L^*, is defined as the ratio of combustor volume to nozzle throat area, it is expected to influence the overall flow condition in the combustor and the velocity-gradient field near the stagnation regions generated by the impinging jets. Therefore, L^* was selected as the principal design parameter in this study. To evaluate the effect of this parameter, combustion tests were conducted using CAMUI-type hybrid rockets with 80 wt% and 70 wt% hydrogen peroxide as oxidizers under non-catalytic spray-injection conditions. In the present experiments, L^* was systematically varied by changing the nozzle throat diameter while maintaining the combustor volume constant. This procedure was adopted because varying the combustor length would change not only L^* but also the wall surface area, heat loss, flow-path length, and residence-time distribution, making it difficult to isolate the effect of L^* on combustion efficiency. The characteristic exhaust velocity efficiency, η_{c^*}, and chamber pressure behavior were then evaluated for each oxidizer concentration. The present results provide a practical design guideline for catalyst-free hydrogen peroxide hybrid rocket motors; in particular, they help determine the minimum L^* that should be ensured to maintain stable and efficient combustion when oxidizer concentration degradation during long-term storage must be considered.

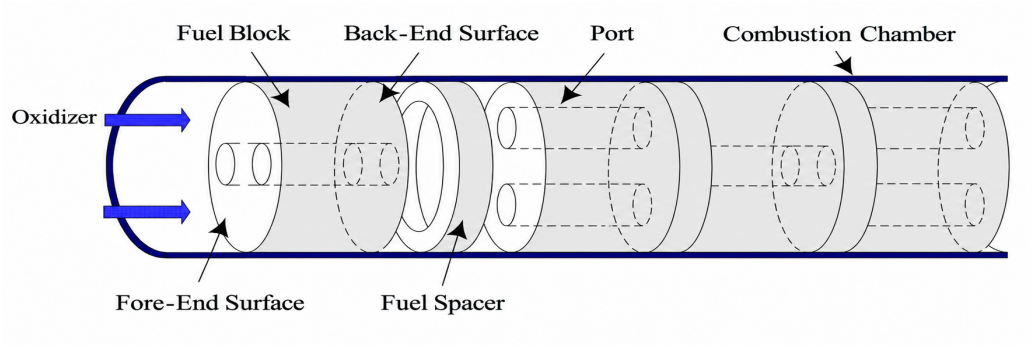


Figure 1. Schematic diagram of CAMUI Fuel.

2. Methods

2.1. Experimental Apparatus

Combustion tests were conducted using 70 wt% and 80 wt% hydrogen peroxide as oxidizers. The experiments were performed using a laboratory-scale hybrid rocket test system developed for hydrogen peroxide operation. The experimental apparatus consisted of an oxidizer tank, an electromagnetic valve, an oxidizer feed line, a combustor assembly, measurement devices, and a data acquisition system. A schematic overview of the test setup is shown in Figure 2.

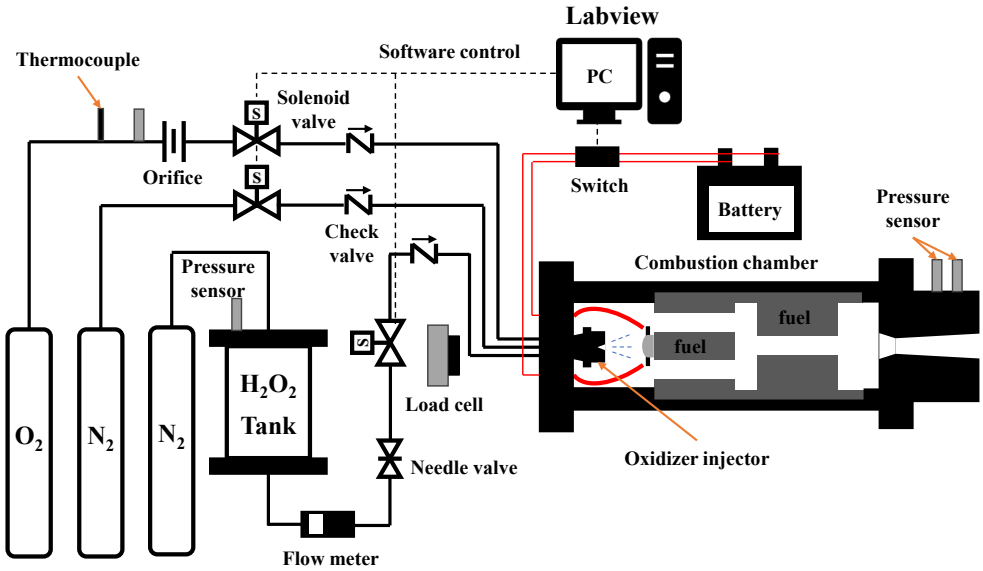


Figure 2. Schematic diagram of the Combustion Test Setup.

Hydrogen peroxide was injected into the combustion chamber from the upstream end through a full-cone nozzle (J010N S303W, H. IKEUCHI & Co., Ltd., Osaka, Japan). The oxidizer flow rate was controlled by an electromagnetic valve. The present test system was therefore configured to evaluate combustion characteristics under non-catalytic spray-injection conditions.

The specifications of the measurement devices used in the combustion tests are summarized in Table 1. The chamber pressure was measured using a pressure transducer (Kyowa Electronic Instruments Co., Ltd., Chofu, Tokyo, Japan) with a measurement range of 0.0–5.0 MPa and an accuracy of ±0.030 MPa. The thrust was measured using a load cell (Kyowa Electronic Instruments Co., Ltd., Chofu, Tokyo, Japan) with a measurement range of 0–50 N and an accuracy of ±0.38 N. The oxidizer flow rate was measured using a clamp-on flowmeter (KEYENCE Corporation, Osaka, Japan) with a measurement range of 0–10 mL/s and an accuracy of ±0.15 mL/s. The initial and final fuel masses were

measured using an FX300I-JA electronic balance (A&D Company, Limited, Tokyo, Japan) with a resolution of ±0.002 g. The data acquisition system was an EDX-100A-4H data logger (Kyowa Electronic Instruments Co., Ltd., Chofu, Tokyo, Japan). The nozzle throat diameter was taken from the manufacturer's inspection certificate, in which the measured throat diameter and its tolerance were provided. These specifications were used as input uncertainties in the uncertainty analysis of η_{c^*}, as described in Section 2.5.

Table 1. Measurement devices and uncertainties used in the combustion tests.

Measured Quantity	Device	Range or Resolution	Uncertainty
Chamber pressure	PHB-A-5MP	0–5 MPa	±0.030 MPa
Thrust	LMB-A-50N	0–50 N	±0.38 N
Oxidizer flow rate	FD-XA1	0–10 mL s^{-1}	±0.15 mL s^{-1}
Fuel mass	FX300I-JA	0–320 g	±0.002 g
Data acquisition	EDX-100A-4H	200 Hz	–

The uncertainties were determined based on the manufacturers' inspection certificates.

Each combustion test was conducted according to a predetermined firing sequence. First, a nichrome wire was energized from $t = 0$ to $t = 25$ s to provide an ignition heat source. Next, a small amount of oxygen was supplied from $t = 10$ to $t = 30$ s. Hydrogen peroxide was injected from $t = 25$ to $t = 32$ s, and this interval was defined as the main combustion period. After the termination of hydrogen peroxide injection, nitrogen purge was initiated at $t = 32$ s to remove residual gas and unreacted species from the system.

2.2. Motor Configuration

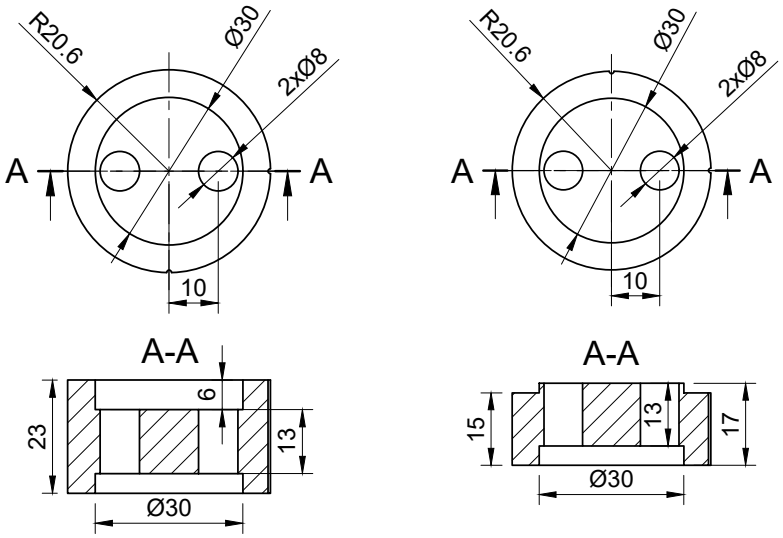
The motor used in this study employed a CAMUI-type fuel grain. The fuel grain was composed of two high-density polyethylene (HDPE) fuel blocks stacked in the axial direction. Each block had a dual-port structure, and the port arrangement was rotated by 90° between successive blocks. This characteristic CAMUI geometry generated alternating jet-impingement and recirculation regions within the combustor. These flow structures enhanced heat transfer to the fuel surface and promoted stagnation-point combustion. A schematic of the CAMUI grain geometry and the combustor cross section is shown in Figures 3 and 4. The motor was configured for hydrogen peroxide combustion under non-catalytic spray-injection conditions. The prechamber and nozzle were fabricated from graphite because of their high thermal resistance.

The characteristic chamber length, L^*, was used as the principal parameter for evaluating the influence of combustor geometry on combustion performance. It was defined as

$$L^* = \frac{V_c}{A_{\mathrm{th}}} \tag{1}$$

where V_c is the combustor volume and A_{th} is the nozzle throat area. In the present experiments, L^* was varied by changing the nozzle throat diameter while maintaining the chamber volume constant.

Combustion tests were conducted using multiple nozzle throat diameters in order to systematically evaluate the relationship between L^* and combustion efficiency.



(**a**) (**b**)

Figure 3. Geometries of the CAMUI fuel blocks used in the present study: (**a**) first-stage fuel block and (**b**) second-stage fuel block. The two blocks were stacked axially with a 90° phase shift to form the CAMUI grain configuration.

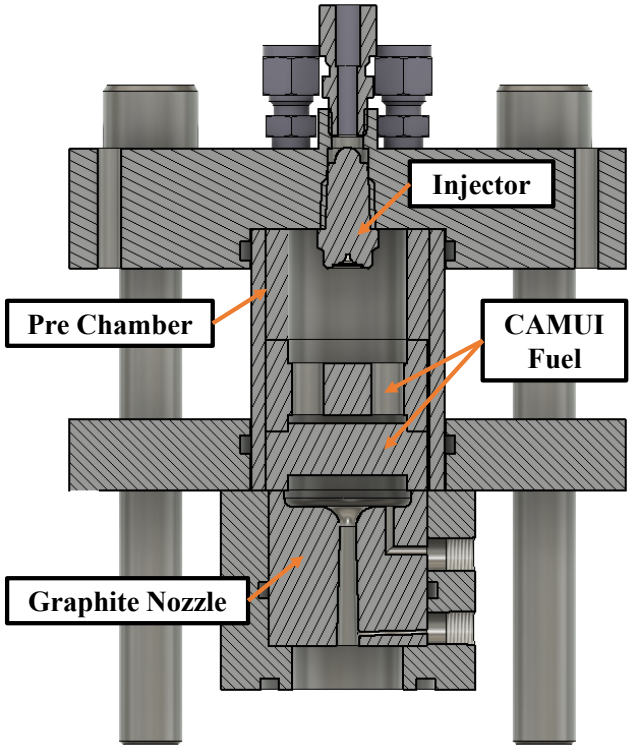


Figure 4. Schematic diagram of the Combustor.

2.3. Data Reduction and Analysis

The characteristic exhaust velocity efficiency, η_{c^*}, was used as the primary performance metric in this study. It was defined as the ratio of the experimental characteristic exhaust velocity, c^*_{ex}, to the theoretical characteristic exhaust velocity, c^*_{th}, as

$$\eta_{c^*} = \frac{c^*_{ex}}{c^*_{th}}. \quad (2)$$

η_{c^*} represents the degree to which the experimentally obtained characteristic exhaust velocity approaches the ideal value, and was used as an index of combustion completion. Values lower than unity indicate losses associated with incomplete combustion, insufficient mixing, heat loss, or other non-ideal effects. The theoretical characteristic exhaust velocity, c^*_{th}, was calculated using NASA CEA [27] under the assumption of chemical equilibrium, with the combustion-period-averaged chamber pressure and oxidizer-to-fuel ratio as inputs. The experimental characteristic exhaust velocity, c^*_{ex}, was calculated from the combustion-period-averaged chamber pressure and propellant mass flow rate as

$$c^*_{\mathrm{ex}} = \frac{\overline{P}_{\mathrm{c}} A_{\mathrm{th}}}{\overline{\dot{m}}_{\mathrm{ox}} + \overline{\dot{m}}_{\mathrm{f}}} \tag{3}$$

where $\overline{P}_{\mathrm{c}}$, $\overline{\dot{m}}_{\mathrm{ox}}$, and $\overline{\dot{m}}_{\mathrm{f}}$ denote the combustion-period-averaged chamber pressure, oxidizer mass flow rate, and fuel mass flow rate, respectively, and A_{th} is the nozzle throat area.

The combustion period used to evaluate these time-averaged quantities was determined from the chamber pressure history, as shown in Figure 5. The combustion start time, t_i, was defined as the first time at which the chamber pressure reached 75% of the maximum chamber pressure, $P_{\mathrm{c,max}}$, during the initial pressure rise. This threshold was used to exclude the ignition transient and the low-pressure period before the establishment of main combustion. The combustion end time, t_f, was defined as the time at which the chamber pressure began to decrease rapidly after the termination of oxidizer supply. The burn duration, t_b, was defined as the interval between t_i and t_f. For the representative case shown in Figure 5, $t_i = 0.101$ s, $t_f = 6.875$ s, and $t_b = 6.774$ s. The chamber pressure and oxidizer mass flow rate were averaged over this same interval. The oxidizer mass flow rate was obtained from the flowmeter measurement, whereas the fuel mass flow rate was determined by dividing the mass loss of the fuel grain during the firing test by t_b. Thus, the same pressure-based combustion period was consistently used to evaluate $\overline{P}_{\mathrm{c}}$, $\overline{\dot{m}}_{\mathrm{ox}}$, $\overline{\dot{m}}_{\mathrm{f}}$, the oxidizer-to-fuel ratio, c^*_{ex}, and η_{c^*}.

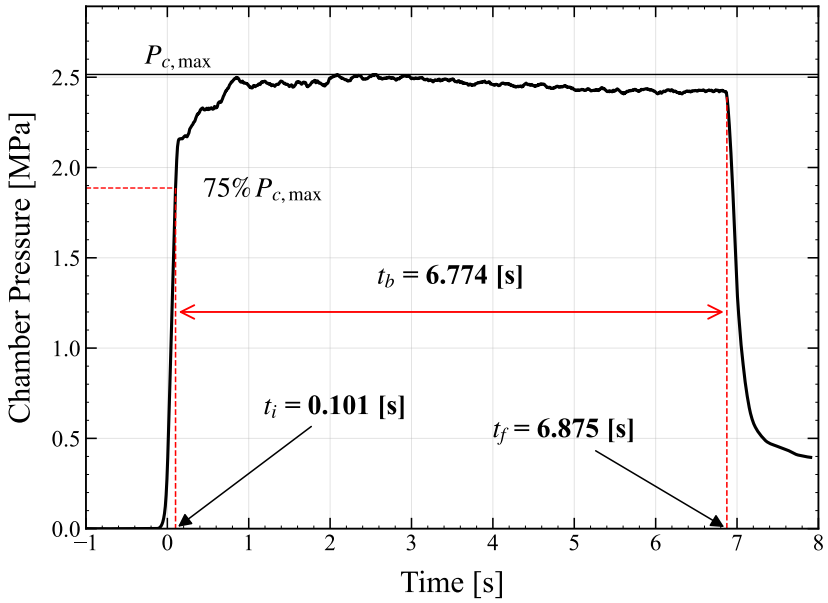


Figure 5. Definition of the combustion period used for data reduction. The combustion start time, t_i, was defined as the first time at which the chamber pressure reached 75% of the maximum chamber pressure, $P_{\mathrm{c,max}}$, during the initial pressure rise. The combustion end time, t_f, was defined as the time at which the chamber pressure began to decrease rapidly after the termination of oxidizer supply. The burn duration, t_b, corresponds to the interval between t_i and t_f.

2.4. Pressure Oscillation Analysis

Pressure oscillations were analyzed to evaluate the combustion stability of each test condition. The objective of this analysis was not to develop a detailed instability model, but to quantify the relative magnitude and frequency characteristics of the chamber pressure fluctuations. The chamber pressure signal was analyzed over the same combustion period, from t_i to t_f, as that used for the data reduction described in Section 2.3.

The magnitude of the pressure oscillation was evaluated using the normalized root-mean-square (RMS) pressure fluctuation, defined as

$$\frac{P'_{\mathrm{rms}}}{\overline{P}_{\mathrm{c}}} = \frac{1}{\overline{P}_{\mathrm{c}}}\sqrt{\frac{1}{N}\sum_{i=1}^{N}\left(P_{\mathrm{c},i} - \overline{P}_{\mathrm{c}}\right)^2} \tag{4}$$

where $P_{\mathrm{c},i}$ is the instantaneous chamber pressure, $\overline{P}_{\mathrm{c}}$ is the combustion-period-averaged chamber pressure, and N is the number of data points within the combustion period. This value was used as a quantitative index of the pressure-oscillation intensity.

Frequency-domain analysis was also performed using the fast Fourier transform (FFT). Prior to the FFT calculation, the mean component was removed from the chamber pressure signal as

$$P'_{\mathrm{c}}(t) = P_{\mathrm{c}}(t) - \overline{P}_{\mathrm{c}} \tag{5}$$

The FFT was then applied to $P'_{\mathrm{c}}(t)$ to obtain the amplitude spectrum of the pressure fluctuation. The zero-frequency component was excluded from the analysis. When a distinct spectral peak was observed, the dominant frequency, f_{dom}, was defined as the frequency corresponding to the largest peak in the amplitude spectrum. In contrast, when the spectrum was dominated by broadband components or very-low-frequency drift without a distinct peak, f_{dom} was not regarded as a definitive indicator of combustion instability.

The normalized RMS pressure fluctuation was therefore used as the primary index for comparing combustion stability among the test cases, whereas the FFT result and f_{dom} were used as auxiliary diagnostic information to identify characteristic oscillation modes when they were clearly observed.

2.5. Uncertainty Analysis of c^* Efficiency

The uncertainty in the c^* efficiency, η_{c^*}, was evaluated by propagating the bias uncertainties introduced by the experimental measurements using the following first-order uncertainty-propagation equation:

$$u_y^2 = \sum_i \left(\frac{\partial y}{\partial x_i} u_{x_i}\right)^2 \tag{6}$$

where y is an output quantity, x_i is an input quantity, and u_{x_i} is the uncertainty associated with x_i. In the present study, $y = \eta_{c^*}$, and the relevant input quantities were the combustion-period-averaged chamber pressure, $\overline{P}_{\mathrm{c}}$, nozzle throat diameter, D_{th}, oxidizer mass flow rate, $\overline{\dot{m}}_{\mathrm{ox}}$, fuel mass flow rate, $\overline{\dot{m}}_{\mathrm{f}}$, and theoretical characteristic exhaust velocity, c^*_{th}. Accordingly, the uncertainty in η_{c^*} was expressed as

$$u_{\eta_{c^*}}^2 = \left(\frac{\partial \eta_{c^*}}{\partial P_{\mathrm{c}}} u_{P_{\mathrm{c}}}\right)^2 + \left(\frac{\partial \eta_{c^*}}{\partial D_{\mathrm{th}}} u_{D_{\mathrm{th}}}\right)^2 + \left(\frac{\partial \eta_{c^*}}{\partial \overline{\dot{m}}_{\mathrm{ox}}} u_{\overline{\dot{m}}_{\mathrm{ox}}}\right)^2 + \left(\frac{\partial \eta_{c^*}}{\partial \overline{\dot{m}}_{\mathrm{f}}} u_{\overline{\dot{m}}_{\mathrm{f}}}\right)^2 + \left(\frac{\partial \eta_{c^*}}{\partial c^*_{\mathrm{th}}} u_{c^*_{\mathrm{th}}}\right)^2 \tag{7}$$

where $u_{(\cdot)}$ denotes the uncertainty associated with the corresponding quantity. The input uncertainties were determined from the specifications and inspection certificates of the measurement devices listed in Table 1. The uncertainty of the chamber pressure was evalu-

ated by combining the pressure-transducer accuracy and the pressure fluctuation during the combustion period. The latter was introduced to account for the uncertainty associated with representing an unsteady chamber pressure history by a single combustion-period-averaged value. Following the approach of Frederick and Greiner [28], this contribution was estimated as one-half of the difference between the maximum and minimum chamber pressures during the combustion period:

$$u_{P,\mathrm{fluc}} = \frac{P_{\mathrm{c,max}} - P_{\mathrm{c,min}}}{2}. \tag{8}$$

The total uncertainty of the averaged chamber pressure was then calculated as

$$u_{\overline{P}_\mathrm{c}} = \sqrt{u_{P,\mathrm{sens}}^2 + u_{P,\mathrm{fluc}}^2}. \tag{9}$$

The oxidizer mass-flow-rate uncertainty was evaluated from the flowmeter uncertainty in the same manner. The uncertainty in the fuel mass consumption was taken as the resolution limit of the electronic balance, since repeated mass measurements showed no observable scatter within the balance resolution. The uncertainty in the fuel mass flow rate was then propagated from the uncertainties in the initial fuel mass, final fuel mass, and burn duration.

The theoretical characteristic exhaust velocity, c^*_{th}, was obtained numerically using NASA CEA [27] and is not available in closed analytical form. Therefore, its sensitivity coefficients were evaluated by finite differences around the nominal operating point for each test condition as

$$\frac{\partial c^*_{\mathrm{th}}}{\partial x_i} \approx \frac{c^*_{\mathrm{th}}(x_i + \Delta x_i) - c^*_{\mathrm{th}}(x_i - \Delta x_i)}{2\Delta x_i}, \qquad x_i \in \{\overline{P}_\mathrm{c}, \mathrm{O/F}\}, \tag{10}$$

where x_i denotes either the combustion-period-averaged chamber pressure, $\overline{P}_\mathrm{c}$, or the oxidizer-to-fuel ratio, O/F, and Δx_i denotes a small perturbation about the nominal value. The uncertainty in c^*_{th} estimated from these sensitivity coefficients was included in the uncertainty propagation for η_{c^*}. The resulting uncertainty in η_{c^*} was used to determine the error bars shown in Section 3.1.

3. Results

Combustion tests were conducted over a wide range of L^* by changing the nozzle throat diameter while maintaining the combustor volume constant. In the 80 wt% series, valid combustion data were obtained for all tested conditions. Table 2 summarizes the principal results of the combustion tests conducted in this study. In Table 2, Conc. denotes the oxidizer concentration; D_{th} is the nozzle throat diameter; L^* is the characteristic chamber length; $\overline{P}_\mathrm{c}$ is the time-averaged chamber pressure; $\overline{\dot{m}}_{\mathrm{ox}}$ and $\overline{\dot{m}}_f$ are the time-averaged oxidizer and fuel mass flow rates, respectively; O/F is the oxidizer-to-fuel mass ratio; c^*_{exp} is the experimental characteristic exhaust velocity; η_{c^*} is the characteristic exhaust velocity efficiency; and $P'_{\mathrm{rms}}/\overline{P}_\mathrm{c}$ is the normalized RMS pressure fluctuation. In the 70 wt% series, combustion data were obtained for most test conditions; however, flame blowoff occurred at $D_{\mathrm{th}} = 4.0\,\mathrm{mm}$, corresponding to $L^* = 2.48\,\mathrm{m}$.

Representative chamber pressure histories for stable combustion using 70 wt% and 80 wt% hydrogen peroxide are shown in Figure 6. In both cases, the chamber pressure increased rapidly after ignition and remained approximately steady during the main combustion period. However, even under the same nozzle throat diameter, the 70 wt% case exhibited somewhat larger pressure fluctuations than the 80 wt% case. These results

suggest that the oxidizer concentration affects not only combustion performance but also the chamber pressure behavior.

In the following sections, the relationship between L^* and η_{c^*} is first presented in Section 3.1. The results of the pressure-oscillation analysis are then presented in Section 3.2.

Table 2. Summary of combustion test results for 70 wt% and 80 wt% H_2O_2.

Test ID	Conc. [wt%]	D_{th} [mm]	L^* [m]	$\overline{P}_c$ [MPaA]	$\overline{\dot{m}}_{ox}$ [g/s]	$\overline{\dot{m}}_f$ [g/s]	O/F	c^*_{exp} [m/s]	η_{c^*}	$P'_{rms}/\overline{P}_c$ [%]
S-5	80.7	2.25	7.81	3.13	5.91	1.94	3.03	1584	1.24	2.54
S-6	80.7	2.50	6.33	2.53	6.49	1.98	3.27	1465	1.12	2.26
S-7	80.7	2.75	5.23	2.27	6.96	2.10	3.31	1485	1.13	2.06
S-8	80.7	3.00	4.40	1.81	7.03	2.00	3.53	1414	1.05	2.60
S-9	80.7	3.25	3.75	1.38	6.55	1.64	3.98	1395	1.00	3.91
S-10	80.7	3.50	3.23	1.24	6.87	1.64	4.17	1398	0.99	4.00
S-11	80.7	3.75	2.82	1.06	6.74	1.36	4.97	1444	0.99	4.37
S-12	80.7	4.00	2.48	0.87	6.64	1.16	5.71	1406	0.95	6.90
S-13	80.7	4.25	2.19	0.75	6.53	1.04	6.28	1404	0.93	5.66
S-14	80.7	4.50	1.96	0.65	6.51	1.05	6.19	1360	0.90	5.61
S-15	80.7	4.75	1.76	0.58	6.50	1.03	6.30	1362	0.90	8.17
S-16	80.7	5.00	1.59	0.52	6.36	1.03	6.17	1383	0.92	6.76
S-18	70.7	2.50	6.33	2.25	6.58	1.07	6.12	1443	1.04	4.29
S-19	70.7	3.25	3.75	1.12	6.83	0.76	8.93	1222	0.85	8.56
S-20	70.7	3.50	3.23	0.84	6.55	0.64	10.17	1117	0.77	17.4
S-21	70.7	3.75	2.82	0.64	6.60	0.50	13.12	998	0.73	15.6
S-22	70.7	4.00	2.48	—	—	—	—	—	—	—
S-23	70.8	2.25	7.81	2.98	6.17	1.47	4.21	1553	1.22	3.76
S-24	70.8	2.75	5.23	1.87	6.84	0.98	7.01	1424	1.01	4.60
S-25	70.8	3.00	4.40	1.48	7.05	0.88	7.99	1322	0.93	6.33

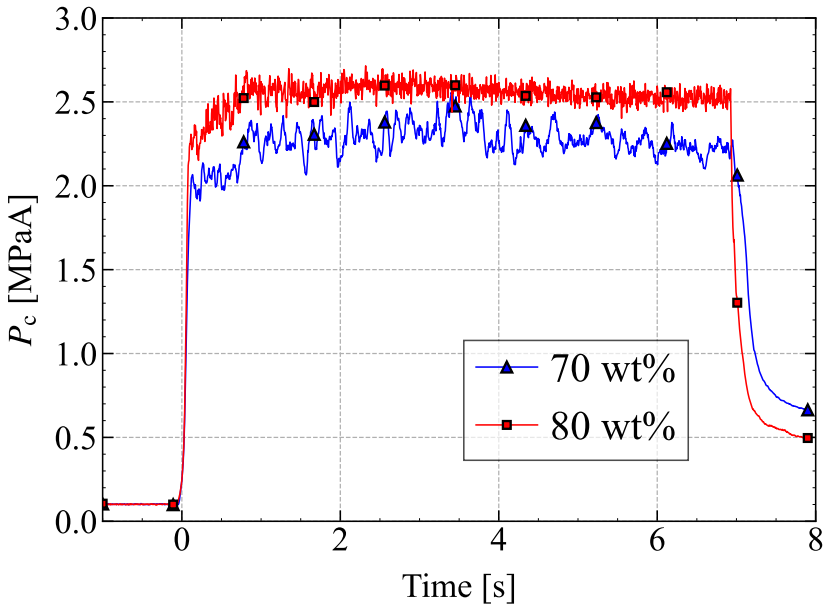


Figure 6. Representative chamber pressure histories for combustion tests at $D_{th} = 2.5$ mm using 70 wt% and 80 wt% H_2O_2.

3.1. Effect of L on c* Efficiency*

Figure 7 shows the relationship between the characteristic chamber length, L^*, and the characteristic exhaust velocity efficiency, η_{c^*}. The error bars represent the propagated

uncertainty in η_{c^*}, as described in Section 2.5. At comparable values of L^*, the 70 wt% cases tended to show lower η_{c^*} than the 80 wt% cases. In the 80 wt% series, relatively high η_{c^*} values were maintained over the tested range of L^*, and the increase in η_{c^*} with increasing L^* was gradual. In contrast, the 70 wt% series showed a stronger dependence of η_{c^*} on L^*. In particular, the decrease in η_{c^*} with decreasing L^* was pronounced in the range of $L^* = 3$–5 m. Furthermore, in the 70 wt% series, valid performance data were obtained down to $L^* = 2.82$ m, whereas flame blowoff occurred at $L^* = 2.48$ m. This result indicates that, under the present combustion conditions, the low-L^* boundary for stable combustion lies between $L^* = 2.48$ m and 2.82 m. As shown in the next section, the 70 wt% series exhibited larger pressure oscillations in the low-L^* region. Therefore, pressure fluctuations during the combustion period contributed to the uncertainty in the time-averaged chamber pressure used to evaluate η_{c^*}, resulting in larger error bars for the low-L^* 70 wt% cases.

In the high-L^* region, corresponding to smaller nozzle throat diameters, several data points exhibited apparent η_{c^*} values exceeding unity for both oxidizer concentrations. These values do not necessarily indicate combustion performance beyond the thermodynamic limit, because the present data reduction used the geometric nozzle throat area. A possible interpretation based on the effective throat area is discussed in Section 4.

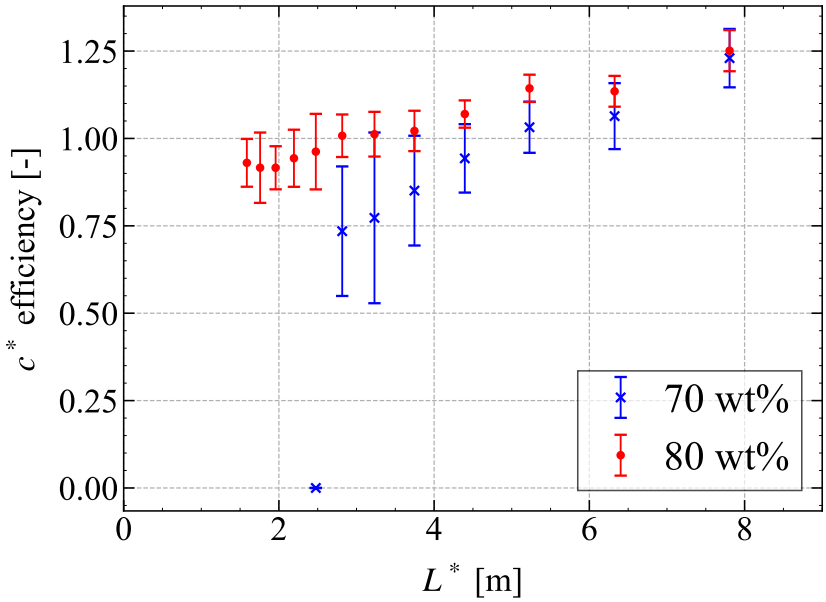


Figure 7. Characteristic exhaust velocity efficiency, η_{c^*}, as a function of L^*, for combustion tests using 70 wt% and 80 wt% H_2O_2. Error bars indicate the uncertainty estimated from the propagated uncertainties of chamber pressure, throat diameter, oxidizer flow rate, fuel mass consumption, and theoretical c^*.

3.2. Pressure Oscillation

Figure 8 shows representative chamber pressure histories for low-L^* combustion tests using 70 wt% hydrogen peroxide. Compared with the stable combustion cases shown in Figure 6, the low-L^* cases exhibited larger pressure oscillations during the combustion period. In particular, large-amplitude pressure fluctuations were observed before flame blowoff at $L^* = 2.48$ m. These pressure histories indicate that the combustion became more unstable as L^* decreased in the 70 wt% cases.

The pressure oscillation intensity was quantified using the normalized RMS pressure fluctuation defined in Section 2.4. Figure 9 shows the normalized RMS pressure fluctuation as a function of L^*. The 80 wt% cases showed relatively small normalized RMS values over the tested range of L^*. In contrast, the 70 wt% cases showed larger normalized RMS

values, particularly in the low-L^* region. Therefore, the comparison of the normalized RMS pressure fluctuation shows that, under the present combustion conditions, the 70 wt% cases were more unstable than the 80 wt% cases.

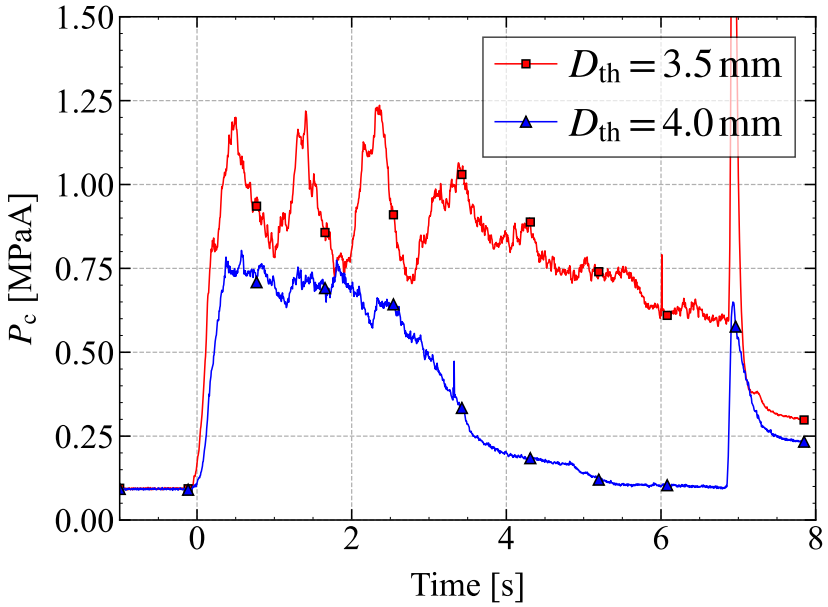


Figure 8. Representative chamber pressure histories for low-L^* combustion tests using 70 wt% H_2O_2. The case at $D_{th} = 3.5$ mm exhibited pronounced pressure oscillations, whereas the case at $D_{th} = 4.0$ mm resulted in flame blowout.

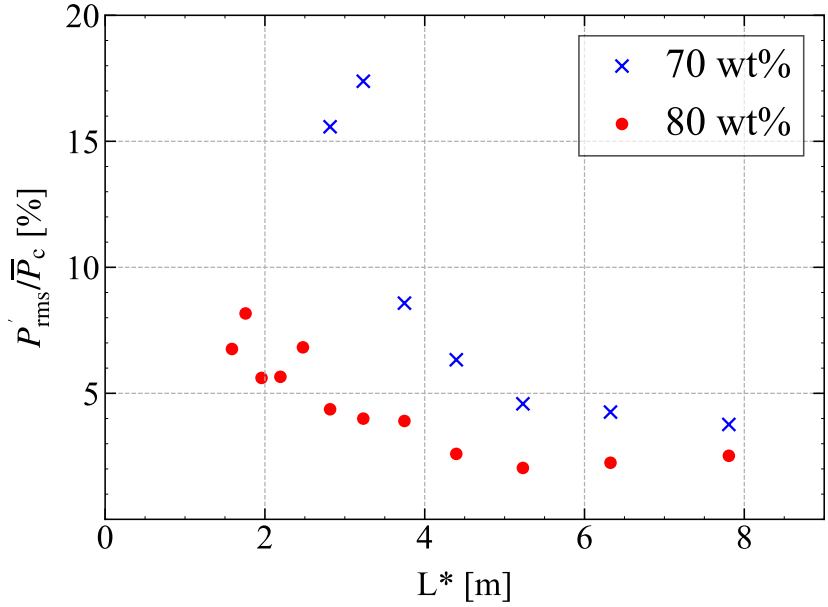


Figure 9. Normalized RMS pressure fluctuation, $P'_{rms}/\overline{P}_c$, as a function of the characteristic chamber length L^* for 70 wt% and 80 wt% hydrogen peroxide. The RMS pressure fluctuation was calculated from the chamber pressure history during the combustion period and normalized by the combustion-period-averaged chamber pressure.

Frequency-domain analysis was also conducted using FFT to examine the characteristic frequency components of the chamber pressure fluctuations. In some 70 wt% cases, low-frequency components were observed in the amplitude spectrum. However, a consistent dominant frequency could not be identified over all test conditions. Some cases showed

distinct low-frequency peaks, whereas others were dominated by broadband components or very-low-frequency drift.

4. Discussion

Based on the experimental results, the discussion is organized around three points: (1) the dependence of the required L^* for high η_{c^*} on oxidizer concentration; (2) the origin of the larger pressure oscillations observed in the 70 wt% cases; and (3) the interpretation of the apparent η_{c^*} values exceeding unity in the high-L^* region.

4.1. Concentration Dependence of L^*

The concentration dependence of the required L^* is discussed here in terms of the combustor scale required for combustion completion. In the present experiments, L^* was varied by changing the nozzle throat diameter while maintaining the combustor volume constant. Although L^* is often used as a design parameter related to the residence-time scale in rocket combustors, it should not be interpreted here as a direct measure of the actual gas residence time. The actual residence time depends on the gas temperature, gas composition, and internal velocity field, none of which were directly measured in the present experiments. Therefore, in this study, L^* is treated as a practical geometric parameter representing the combustor scale available for oxidizer heating, vaporization, decomposition, mixing with fuel-rich gas, and heat release.

The concentration dependence observed in the experimental results can be interpreted from the thermophysical characteristics of hydrogen peroxide solutions. As the oxidizer concentration decreases from 80 wt% to 70 wt%, the water fraction increases. Consequently, the heat required for heating and vaporization becomes larger, while the heat released by exothermic decomposition becomes smaller. According to reported thermophysical values [29], the heat required to heat and vaporize the liquid oxidizer is approximately 1830 J/g for 70 wt% hydrogen peroxide and 1740 J/g for 80 wt% hydrogen peroxide. The heat released by exothermic decomposition decreases more significantly, from approximately 753 J/g for 80 wt% hydrogen peroxide to 335 J/g for 70 wt% hydrogen peroxide. These values are used here as reference values for comparing the two oxidizer concentrations, rather than as a direct quantitative model of the combustion process. In the actual combustor, oxidizer heating, vaporization, decomposition, mixing, and heat release proceed simultaneously in a high-temperature reacting flow field. A rigorous evaluation of these processes would require direct measurements of spray characteristics, gas temperature, gas composition, and local flow fields, or a detailed multiphase reacting-flow analysis. Nevertheless, the thermophysical comparison indicates that 70 wt% hydrogen peroxide imposes a larger thermal burden before vaporization, decomposition, mixing, and heat release can proceed sufficiently. Therefore, the observed shift of the required L^* toward larger values in the 70 wt% cases is consistent with the interpretation that lower-concentration hydrogen peroxide requires a larger geometric combustor scale for combustion completion.

4.2. Pressure Oscillation and Combustion Stability Under Lower-Concentration Conditions

The pressure oscillation and combustion stability under lower-concentration conditions are discussed in this subsection. The pressure-oscillation analysis showed that the normalized RMS pressure fluctuation increased as L^* decreased, and that the 70 wt% cases tended to exhibit larger RMS values than the 80 wt% cases. This result quantitatively indicates that lower-concentration hydrogen peroxide is more susceptible to unsteady chamber pressure behavior, particularly in the low-L^* region.

A possible reason for the larger pressure oscillations observed in the 70 wt% cases is that the spray condition provided by the same injector became relatively less favorable

for stable combustion as the oxidizer concentration decreased. Previous studies have compared chamber pressure histories obtained with finer and coarser injectors under the same hydrogen peroxide concentration and reported that coarser oxidizer droplets induced stronger pressure oscillations, whereas finer atomization stabilized the chamber pressure and improved combustion efficiency [30]. This indicates that the spray scale can significantly affect pressure stability in hydrogen peroxide hybrid rocket combustion. As discussed in the previous subsection, 70 wt% hydrogen peroxide requires a larger heat input for heating and vaporization and releases less heat through exothermic decomposition than 80 wt% hydrogen peroxide. Consequently, a spray condition that was sufficient to maintain stable heat release for 80 wt% hydrogen peroxide may have provided a smaller stability margin for 70 wt% hydrogen peroxide, where vaporization, decomposition, mixing, and heat release must proceed under a larger thermal burden. This interpretation does not imply that the droplet size was larger in the 70 wt% cases. Rather, it suggests that the same injector and spray condition may have been relatively less favorable for the lower-concentration oxidizer. This effect is expected to become more pronounced in the low-L^* region, where the geometric combustor scale available for vaporization, decomposition, mixing, and heat release is reduced. A temporary reduction in heat release can decrease the chamber pressure and weaken flame holding in the recirculation and impingement regions of the CAMUI combustor. Such coupling between heat-release fluctuations and chamber pressure response provides a plausible explanation for the larger RMS pressure fluctuations observed in the low-L^* 70 wt% cases.

It should be emphasized that this interpretation is not a direct identification of the instability mechanism. In the present experiments, spray characteristics, droplet-scale evaporation, gas temperature, gas composition, and local heat-release distributions were not measured. Therefore, the pressure-oscillation analysis demonstrates that larger unsteady pressure behavior occurred under lower-concentration conditions, while the thermophysical comparison indicates that this behavior is consistent with the more demanding combustion-completion process of 70 wt% hydrogen peroxide.

4.3. Interpretation of Apparent η_{c^*} Values Exceeding Unity

The apparent η_{c^*} values exceeding unity observed in the high-L^* region are examined in terms of the effective nozzle throat area. In the present data reduction, η_{c^*} was evaluated using the geometric throat area. However, during firing, the effective throat area can be smaller than the geometric area because of boundary-layer displacement at the nozzle throat. When the geometric throat area is used in this situation, the experimental characteristic exhaust velocity is overestimated. For the S-5 case, the effective throat radius required to reduce the apparent characteristic exhaust velocity efficiency to $\eta_{c^*} = 1.0$ was estimated from the measured chamber pressure and propellant mass flow rate. This calculation gave a radial reduction of approximately 0.118 mm relative to the geometric throat radius. This value can be interpreted as the order of the throat displacement thickness required to explain the apparent $\eta_{c^*} > 1.0$. Sibulkin reported boundary-layer measurements at supersonic nozzle throats and showed that turbulent boundary layers exist at the throat, with measured displacement thicknesses on the order of 0.0054–0.0130 in. (0.14–0.33 mm) [31]. Therefore, the 0.118 mm correction estimated in the present study is of the same order as experimentally observed throat displacement thicknesses. This comparison suggests that the apparent $\eta_{c^*} > 1.0$ values observed in the high-L^* region can be explained, at least in part, by the reduction of the effective throat area due to the nozzle-throat boundary layer. Therefore, these values should not be interpreted as combustion performance exceeding the thermodynamic limit.

5. Conclusions

This study experimentally investigated the effects of characteristic chamber length, L^*, on the combustion efficiency and stability of CAMUI-type hybrid rockets using 70 wt% and 80 wt% hydrogen peroxide under non-catalytic spray-injection conditions. The main novelty of this work is that it clarified the concentration-dependent L^* requirement for catalyst-free hydrogen peroxide hybrid rocket combustion by systematically varying L^* while maintaining the combustor volume constant.

The experimental results showed that η_{c^*} increased with increasing L^* for both oxidizer concentrations, while the 70 wt% cases required a larger L^* than the 80 wt% cases to achieve comparable combustion efficiency. In the 70 wt% series, the lower-L^* boundary for stable combustion was found to lie between $L^* = 2.48$ m and $L^* = 2.82$ m under the present combustion conditions. The pressure-oscillation analysis further showed that lower-concentration hydrogen peroxide is more susceptible to unstable chamber pressure behavior, particularly in the low-L^* region. These trends are consistent with the larger thermal burden for heating and vaporization and the smaller heat release from exothermic decomposition in 70 wt% hydrogen peroxide.

The principal contribution of this study is to provide an experimental design guideline for catalyst-free hybrid rocket motors using medium- or lower-concentration hydrogen peroxide. From the viewpoint of combustor configuration, the present results suggest that 70 wt% hydrogen peroxide should not be operated in the low-L^* region, where flame blowoff and large pressure oscillations are more likely to occur under the present configuration. A preferable configuration is one in which L^* is sufficiently large to achieve high η_{c^*} while maintaining low normalized RMS pressure fluctuation. Therefore, further optimization of the combustor geometry and injector conditions will be required to determine the optimal configuration for low-concentration hydrogen peroxide operation. As an important outcome of this study, the present results demonstrate that stable and efficient combustion of 70 wt% hydrogen peroxide can be achieved in a CAMUI-type combustor without catalytic assistance when a sufficiently large L^* is provided. These findings contribute to moving hydrogen peroxide hybrid rocket design away from catalyst-dependent architectures and toward simpler propulsion systems. In addition, because the proposed approach does not require a catalyst bed, it can avoid reliability issues associated with catalyst degradation, ageing, thermal shock, and pressure loss. This contribution is significant for the development of safer, simpler, and more reliable hybrid propulsion systems for small spacecraft, particularly in applications where oxidizer concentration degradation during long-term storage must be considered.

Author Contributions: Conceptualization, R.K., M.W. and H.N.; Methodology, R.K.; Software, R.K.; Validation, R.K.; Formal analysis, R.K.; Investigation, R.K., S.W. and A.R.D.; Data curation, R.K.; Writing – original draft, R.K.; Writing – review & editing, R.K., M.W. and H.N.; Visualization, R.K.; Supervision, H.N.; Project administration, R.K. and H.N.; Funding acquisition, H.N. All authors have read and agreed to the published version of the manuscript.

Funding: This research was funded by the Innovative Science and Technology Initiative for Security (Grant Number JPJ004596), ATLA, Japan.

Data Availability Statement: The original contributions presented in the study are included in the article, further inquiries can be directed to the corresponding author.

Acknowledgments: The authors would like to thank the members of the LSS (Laboratory of Space System) at Hokkaido University for their assistance in designing the experimental setup and for valuable technical discussions. The authors also thank all colleagues who supported the preparation and execution of the combustion tests.

Conflicts of Interest: H.N. serves as Chief Technology Officer of Letara Ltd. and receives compensation from the company. S.W. and A.R.D. are employed part-time by Letara Ltd. Letara Ltd. conducts research and development on hybrid rocket propulsion. The findings of this manuscript may be relevant to future commercialization activities in this field. These relationships did not influence the design of the study; the collection, analysis, or interpretation of data; the writing of the manuscript; or the decision to publish the results. The other authors declare no conflicts of interest. The funders had no role in the design of the study; the collection, analysis, or interpretation of data; the writing of the manuscript; or the decision to publish the results.

References

1. Kopacz, J.R.; Herschitz, R.; Roney, J. Small Satellites an Overview and Assessment. *Acta Astronaut.* **2020**, *170*, 93–105. [CrossRef]
2. BryceTech. *Orbital Launches Year in Review 2025*; Technical Report; BryceTech: Alexandria, VA, USA, 2026.
3. Barato, F.; Toson, E.; Milza, F.; Pavarin, D. Investigation of Different Strategies for Access to Space of Small Satellites on a Defined LEO Orbit. *Acta Astronaut.* **2024**, *222*, 11–28. [CrossRef]
4. Sutton, G.P.; Biblarz, O. *Rocket Propulsion Elements*, 9th ed.; John Wiley & Sons: Hoboken, NJ, USA, 2017.
5. Altman, D.; Holzman, A. Overview and History of Hybrid Rocket Propulsion. In *Fundamentals of Hybrid Rocket Combustion and Propulsion*; Chiaverini, M.J., Kuo, K.K., Eds.; Progress in Astronautics and Aeronautics, Vol. 218; American Institute of Aeronautics and Astronautics: Reston, VA , USA, 2007; pp. 1–36. [CrossRef]
6. Kamps, L.; Hirai, S.; Nagata, H. Hybrid Rockets as Post-Boost Stages and Kick Motors. *Aerospace* **2021**, *8*, 253. [CrossRef]
7. Shanley, E.S.; Greenspan, F.P. Highly Concentrated Hydrogen Peroxide: Physical and Chemical Properties. *Ind. Eng. Chem.* **1947**, *39*, 1536–1543. [CrossRef]
8. Zhao, B.; Yu, N.; Liu, Y.; Zeng, P.; Wang, J. Unsteady simulation and experimental study of hydrogen peroxide throttleable catalyst hybrid rocket motor. *Aerosp. Sci. Technol.* **2018**, *76*, 27–36. [CrossRef]
9. Li, C.; Cai, G.; Wang, P.; Tian, H. Flow field and injector heat characteristics of hybrid rocket motor with annular-gap injector. *Aerosp. Sci. Technol.* **2019**, *93*, 105326. [CrossRef]
10. Ahn, B.; Kang, H.; Lee, E.; Yun, Y.; Kwon, S. Design of Multiport Grain with Hydrogen Peroxide Hybrid Rocket. *J. Propuls. Power* **2018**, *34*, 1189–1197. [CrossRef]
11. Franco, M.; Barato, F.; Paccagnella, E.; Santi, M.; Battiston, A.; Comazzetto, A.; Pavarin, D. Regression Rate Design Tailoring Through Vortex Injection in Hybrid Rocket Motors. *J. Spacecr. Rocket.* **2020**, *57*, 278–290. [CrossRef]
12. Stella, M.; Zeni, L.; Nichelini, L.; Bellomo, N.; Pavarin, D.; Migliorino, M.T.; Fabiani, M.; Bianchi, D.; Nasuti, F.; Paravan, C.; et al. Experimental Investigation of a H2O2 Hybrid Rocket with Different Swirl Injections and Fuels. *Appl. Sci.* **2024**, *14*, 5625. [CrossRef]
13. Jeong, J.; Bhosale, V.K.; Kwon, S. Ultrafast igniting, low toxicity hypergolic hybrid solid fuels and hydrogen peroxide oxidizer. *Fuel* **2021**, *286*, 119307. [CrossRef]
14. Deng, L.; Ping, L.; Chen, C.; Wang, W.; Zhang, G.; Yang, Y. Numerical analysis of hydrogen peroxide injection effect on the combustion characteristics of a staged combustion aft-injected hybrid rocket motor. *Acta Astronaut.* **2025**, *234*, 429–444. [CrossRef]
15. Okninski, A.; Surmacz, P.; Bartkowiak, B.; Mayer, T.; Sobczak, K.; Pakosz, M.; Kaniewski, D.; Matyszewski, J.; Rarata, G.; Wolanski, P. Development of Green Storable Hybrid Rocket Propulsion Technology Using 98% Hydrogen Peroxide as Oxidizer. *Aerospace* **2021**, *8*, 234. [CrossRef]
16. Faenza, M.G.; Boiron, A.J.; Haemmerli, B.; Verberne, O. Development of the Nucleus Hybrid Propulsion System: Enabling A Successful Flight Demonstration. In Proceedings of the AIAA Propulsion and Energy 2019 Forum, Indianapolis, IN, USA, 19–22 August 2019; AIAA 2019-3839. [CrossRef]
17. Kang, S. Performance analysis of catalyst bed in hydrogen peroxide hybrid rocket. *CEAS Space J.* **2025**, *17*, 901–916. [CrossRef]
18. Parzybut, A.; Surmacz, P.; Gut, Z. Impact of Hydrogen Peroxide Concentration on Manganese Oxide and Platinum Catalyst Bed Performance. *Aerospace* **2023**, *10*, 556. [CrossRef]
19. Mezyk, L.; Kindracki, J.; Wacko, K.; Wozniak, P.; Kostecki, M.; Petrus, M.; Surmacz, P.; Bel, F.V. Initial investigation of catalyst pack for 98%+ hydrogen peroxide satellite monopropellant thruster. *Acta Astronaut.* **2024**, *225*, 913–927. [CrossRef]
20. Cottenot, C.; Beauchet, R.; Boust, B.; Prevost, L.; Batonneau, Y.; Bellenoue, M. Influence of hydrogen peroxide catalyst grain size on performance and ageing. *Acta Astronaut.* **2025**, *226*, 332–340. [CrossRef]
21. Ventura, M.C. Long Term Storability of Hydrogen Peroxide. In Proceedings of the 41st AIAA/ASME/SAE/ASEE Joint Propulsion Conference & Exhibit, Tucson, AZ, USA, 10–13 July 2005; AIAA 2005-4551. [CrossRef]
22. Wernimont, E.J.; Heister, S.D. Combustion Experiments in Hydrogen Peroxide/Polyethylene Hybrid Rocket with Catalytic Ignition. *J. Propul. Power* **2000**, *16*, 318–326. [CrossRef] [PubMed]

23. Whitmore, S.A.; Marshall, J.; Bulcher, M.; Lui, L.; Heiner, M.; Chamberlain, B.; Martinez, C.; Armstrong, I.; Merkley, D.P. Arc-Ignition of a 70%–80% Hydrogen Peroxide/ABS Hybrid Rocket System. In Proceedings of the 53rd AIAA/SAE/ASEE Joint Propulsion Conference, Atlanta, GA, USA, 10–12 July 2017; AIAA 2017-5047. [CrossRef]
24. Nagata, H.; Ito, M.; Maeda, T.; Watanabe, M.; Uematsu, T.; Totani, T.; Kudo, I. Development of CAMUI Hybrid Rocket to Create a Market for Small Rocket Experiments. *Acta Astronaut.* **2006**, *59*, 253–258. [CrossRef]
25. Wakita, M.; Takada, Y.; Iwanaga, K.; Iizuka, T.; Nagata, H. Application of Low Concentration Hydrogen Peroxide for Hybrid Rocket Propulsion System for Small Spacecraft. In Proceedings of the AIAA AVIATION 2022 Forum, Chicago, IL, USA and Virtual, 27 June–1 July 2022; AIAA 2022-3858. [CrossRef]
26. Gallo, G.; Bancalso, L.; Sakurai, H.; Nagata, H. Experiments and Simulations of the Cascaded Multi-Stage Impinging Jet Fuel Combustion in Solid Fuel Ramjets. In Proceedings of the AIAA SciTech 2026 Forum, Orlando, FL, USA, 12–16 January 2026; AIAA 2026-1580. [CrossRef]
27. Gordon, S.; McBride, B.J. *Computer Program for Calculation of Complex Chemical Equilibrium Compositions and Applications*; Technical Report NASA Reference Publication 1311; NASA: Washington, DC, USA, 1994.
28. Frederick, R. A., Jr.; Greiner, B.E. Laboratory-Scale Hybrid Rocket Motor Uncertainty Analysis. *J. Propul. Power* **1996**, *12*, 605–611. [CrossRef]
29. Chemical and Material Sciences Department, Research Division, Rocketdyne, a Division of North American Aviation, Inc. *Hydrogen Peroxide Handbook*; Technical Report AFRPL-TR-67-144; Air Force Rocket Propulsion Laboratory: Edwards, CA, USA, 1967.
30. Anthoine, J.; Lestrade, J.Y.; Messineo, J.; Casu, S. Performances of a Multi-Pulsed Hybrid Rocket Engine Operating with Highly Concentrated Hydrogen Peroxide. In Proceedings of the 53rd AIAA/SAE/ASEE Joint Propulsion Conference, Atlanta, GA, USA, 10–12 July 2017; AIAA 2017-4906. [CrossRef]
31. Sibulkin, M. Boundary-Layer Measurements at Supersonic Nozzle Throats. *J. Aeronaut. Sci.* **1957**, *24*, 249–252. [CrossRef]

Disclaimer/Publisher's Note: The statements, opinions and data contained in all publications are solely those of the individual author(s) and contributor(s) and not of MDPI and/or the editor(s). MDPI and/or the editor(s) disclaim responsibility for any injury to people or property resulting from any ideas, methods, instructions or products referred to in the content.